Published in final edited form as:
J Pathol. 2015 February ; 235(3): 431–444. doi:10.1002/path.4432.

Mycobacterium tuberculosis dysregulates MMP/TIMP balance to drive rapid cavitation and unrestrained bacterial proliferation

André Kübler[1,2], **Brian Luna**[2], **Christer Larsson**[3], **Nicole C. Ammerman**[4], **Bruno B. Andrade**[5], **Marlene Orandle**[6], **Kevin W. Bock**[6], **Ziyue Xu**[7], **Ulas Bagci**[7], **Daniel J. Molura**[7], **John Marshall**[8], **Jay Burns**[9], **Kathryn Winglee**[2], **Bintou Ahmadou Ahidjo**[2,12], **Laurene S. Cheung**[2], **Mariah Klunk**[10], **Sanjay K. Jain**[2,10], **Nathella Pavan Kumar**[13,14], **Subash Babu**[13,15], **Alan Sher**[5], **Jon S. Friedland**[1], **Paul T. G. Elkington**[1,11], and **William R. Bishai**[2,12]

[1]Infectious Diseases & Immunity, Imperial College London, London, UK

[2]Center for Tuberculosis Research, Johns Hopkins University School of Medicine, Baltimore, MD, USA

[3]Department of Molecular Biology, Umeå University, Sweden

[4]KwaZulu-Natal Research Institute for Tuberculosis and HIV (K-RITH), Durban, South Africa

[5]Immunobiology Section, Laboratory of Parasitic Diseases, National Institutes of Allergy and Infectious Diseases, National Institutes of Health, Bethesda, MD, USA

[6]Infectious Diseases Pathogenesis Section, Comparative Medicine Branch, National Institutes of Allergy and Infectious Disease, National Institutes of Health, Bethesda, MD, USA

[7]Radiology and Imaging Science, National Institutes of Health, Bethesda, MD, USA

[8]Johns Hopkins School of Medicine, Baltimore, MD, USA

[9]Biomedical Engineering, Johns Hopkins University, Baltimore, MD, USA

[10]Center for Infectious Disease and Inflammation Imaging Research (CI3R), Baltimore, MD, USA

[11]Faculty of Medicine, Southampton University, UK

[12]Howard Hughes Medical Institute, Chevy Chase, Baltimore, MD, USA

[13]National Institutes of Health, International Center for Excellence in Research, Chennai, India

[14]National Institute for Research in Tuberculosis (NIRT), Chennai, India

Corresponding author: William R. Bishai: Johns Hopkins Center for TB Research, CRB-2 Room 108, 1550 Orleans St, Baltimore, MD 1287, USA. Phone: 1-410-955-3507, wbishai1@jhmi.edu.

Author Contributions

AK and BL contributed equally to the work. Senior authors JSF, PTGE and WRB contributed equally to the work. AK, BL, CL, NCA, JSF, PTGE and WRB designed and performed the experiments. BBA, KWB and MO performed histopathological analysis. ZX. UB, DJM, MK, SKJ, BL and AK contributed to image acquisition and analysis. JB and AK designed and manufactured the breath-hold chamber. JM, KW, BAA, LC, BL, AK, CL and NCA performed rabbit experiments. BBA, NPK, SB and AS acquired human samples and performed analysis. AK prepared the manuscript.

All authors declare that there are no conflicts of interest.

[15]Helminth Immunology Section, Laboratory of Parasitic Diseases, National Institute of Allergy and Infectious Diseases, National Institutes of Health, Bethesda, Maryland, United States of America

Abstract

Active tuberculosis (TB) often presents with advanced pulmonary disease, including irreversible lung damage and cavities. Cavitary pathology contributes to antibiotic failure, transmission, morbidity and mortality. Matrix metalloproteinases (MMPs), in particular MMP-1 are implicated in TB pathogenesis. We explored the mechanisms relating MMP/TIMP imbalance to cavity formation in a modified rabbit model of cavitary TB. Our model results in consistent progression of consolidation to human-like cavities (100% by day 28) with resultant bacillary burdens (>10^7 CFU/g) far greater than those found in matched granulomatous tissue (10^5 CFU/g). Using a novel, breath-hold computerized tomography scanning and image analysis protocol. We show that cavities develop rapidly from areas of densely consolidated tissue. Radiological change correlated with a decrease in functional lung tissue as estimated by changes in lung density during controlled pulmonary expansion (R^2=0.6356, p<0.0001). We demonstrated that the expression of interstitial collagenase (MMP-1) is specifically greater in cavitary compared to granulomatous lesions (p<0.01), and that TIMP-3 significantly decreases at the cavity surface. Our findings demonstrate that an MMP-1/TIMP imbalance, is associated with the progression of consolidated regions to cavities containing very high bacterial burdens. Our model provided mechanistic insight, correlating with human disease at the pathological, microbiological and molecular levels,. It also provides a strategy to investigate therapeutics in the context of complex TB pathology. We used these findings to predict a MMP/TIMP balance in active TB; and confirmed this in human plasma, revealing the potential of MMP/TIMP levels as key components of a diagnostic matrix aimed at distinguishing active from latent TB (PPV=92.9%; 95%CI 66.1–99.8%, NPV=85.6%; 95%CI 77.0–91.9%).

Keywords

Tuberculosis; Matrix Metalloproteinase; Computed tomography; Cavity

Introduction

Tuberculosis (TB) is a leading cause of death worldwide, costing the global economy 100–300 billion dollars, and orphaning 10 million children annually [1–3]. The majority of disease results from *M. tuberculosis* infection of immunocompetent adults, characterized by complex destructive immunopathology, including cavity formation [1, 4–6]. Cavities contain the majority of the bacillary burden in human disease, and play a pivotal role in disease transmission [7, 8]. Within the cavity, immune responses are impaired and antibiotic efficacy altered; treatment failure occurs in up to 15.8% of patients with cavities, compared to just 2.6% of those without [7, 9–11]. Despite this critical role in TB pathogenesis, cavity formation is poorly understood.

Cavitary TB is associated with delayed-type hypersensitivity (DTH) reactions, which are functionally assessed with tuberculin skin tests (TST) [12, 13]. DTH contributes to effective

bacterial control and tissue destruction [14]. Differentiating destructive from antibacterial mechanisms is essential for the development of safe vaccines and immunotherapies. Matrix metalloproteinases (MMPs) are emerging as central mediators of the tissue destructive response in TB [15, 16]. MMPs can cleave all extracellular matrix (ECM) components [6]. In humans MMP-1, which can degrade the most resilient fibrillar components of the ECM (type I and III collagen), and its activator MMP-3, are more abundant in respiratory secretions of TB patients than controls [15, 17, 18]. Conversely, their inhibitors, the tissue inhibitors of metalloproteinases (TIMPs), are not substantially increased [15, 18]. In *M. tuberculosis* infected MMP-1 transgenic mice, collagen degradation is greater than in controls, although these mice do not develop cavities. Possibly because mice have limited functional DTH-responses as determined by responsiveness to PPD after infection (a maximal 0.3mm swelling occurred after injection of 10,000 tuberculin units [TU])[13–15, 19]. These data suggests a dual importance of DTH and pulmonary MMP-1 expression. Investigation of the underlying mechanisms of this relationship are challenging because cavity formation does not occur in *in vitro*, mouse, guinea pig or zebrafish models of TB, and is sporadic in other models [20, 21]. Rabbits and macaques infected with *M. tuberculosis* develop DTH responses, and also occasionally develop cavities [20, 22]. Like humans, these animals can also contain infection [23]. The most consistent cavitary TB model is a post-primary rabbit model, in which DTH responses are induced via presensitization [24]. This model required prolonged infection times and disease progression was inconsistent, leading to difficulties in quantifying outcomes [24, 25].

We developed a reliable model of cavitary disease in rabbits, and confirmed pathological and molecular correlates of human disease. We designed an *in vivo* imaging strategy to observe and quantify the events leading to cavitation. We show that cavities develop rapidly within areas of dense consolidation. This was associated with an MMP-1/TIMP imbalance and high intracavitary bacterial burdens. We provide evidence that *M. tuberculosis* specifically induces MMP-1/-3 and that MMP/TIMP imbalance is a feature of active TB.

Methods

Extended methods are included in Supplementary Information

Mycobacterial Culture

M. tuberculosis H37Rv and *M. bovis* ravenel were grown as in [24].

Animals

3–3.5kg female New Zealand rabbits (Covance research products [Princeton, NJ, USA]) were housed in accordance with protocols [Institutional Animal Care and Use Committee at Johns Hopkins University, (Baltimore, USA)].

Sensitization and infection

As in [24], except: (i) 10^8 instead of 10^7 bacilli were used per presensitization injection, (ii) a target of inoculum of 10^3 CFU was utilized, (iii) Intradermal injection of 0.1ml purified protein derivative (5TU) (Tubersol, Sanofi-Aventis, Bridgewater, NJ, USA) was used to

assess DTH. Briefly, sensitization was achieved using 5 injections of *M. bovis* equally spaced over 14 days and infection with *M. tuberculosis* occurred 21 days later.

Lung sampling

Within 5 minutes of euthanasia [described in [24]], tissue biopsies were taken. Macroscopically matched samples were dissected by gross appearance and: (i) snap frozen in liquid nitrogen (ii) transferred to RNAlater (Invitrogen/Life Technologies, Carlsbad, CA, USA) (iii) fixed in 10% formalin, (iv) 3mm punch biopsies (6 per tissue type per animal) were weighed, homogenized in PBS prior to CFU enumeration on 7H11 selective media. The remaining lung lobe (>90% by mass) was weighed homogenized using a Polytron homogenizer (Kinematica, CH) in 40ml of PBS prior to CFU enumeration by serial dilution on selective 7H11 media.

Rabbit Imaging

Breathhold image acquisition took place as in supplementary Figure 3. Image analysis is described in Supplementary Figures 4, 6 and 7. Tissue type rules described in [26]. Calculations of lung mass was performed as described in supplementary figure 5 and (40).

qPCR

qPCR was performed on 0.5μg/μl RNA samples converted to cDNA using superscript cDNA synthesis kit (Agilent Technologies) according to manufacturers protocols with an additional DNAse incubation. Expression was measured utilizing SYBR II (Bio-Rad, Hercules, CA, USA) and an iQ5 platform (Bio-Rad)(primers: Supplementary Table 2) and and $-\Delta\Delta CT$ and fold changes calculated.

Zymography

Homogenized, sterile-filtered samples were assessed with casein zymograpy [27].

Histology

Tissues was processed by Histoserv and imaged on an Olympus BX51 microscope and photomicrographs were taken using an Olympus DP70 camera.

Ethics

Written informed consent was obtained from all participants, and the study was performed in accordance with the principles expressed in the Declaration of Helsinki and approved by the Institutional Review Board (IRB) of the National Institute for Research in Tuberculosis (NIRT, protocol numbers: NCT01154959 and NCT00342017).

Study population

Cryopreserved heparinized plasma samples were collected from 97 subjects with active pulmonary TB (PTB), 14 with latent TB infection (LTBI) and 20 matched uninfected healthy controls (HC) described in detail in [28].

Immunoassays

Human MMP-1, MMP-3, MMP-7, MMP-8, MMP-9, TIMP-1, TIMP-2, TIMP-3 and TIMP-4 were measured in plasma samples using a luminex kit from R&D systems (R&D Systems, Minneapolis, MN). Rabbit MMP-1 was measured using a commercialized ELISA kit (SEA097Rb; USCN Life Sciences Inc., Hubei, China).

In vitro experiments

Performed as in [27], UV-killed *M. tuberculosis* generated by 90 minutes of UV transillumination (wavelength 365nm, UVP, Upland, CA, USA).

Data analysis

Data analysis was performed as described in the figures using JMP 11 (SAS, Cary, NC), STATA 10 (StataCrop LP, College Station, TX) and Prism 6.0 (GraphPad Software, San Diego, CA). (496)

Results

High-dose pre-sensitization causes rabbit skin test positivity and is required for pulmonary cavity formation

First, we developed a high-dose sensitization regime with heat-killed *Mycobacterium bovis*, since we hypothesized that this would generate cavities more reproducibility than previous studies [24, 29]. This regimen resulted in universal skin-test positivity (Figure 1A and supplementary Table 1) whereas lower dose sensitization did not (data not shown). Cavity formation, detected by serial CT scanning, occurred in all rabbits (Figure 1B and C) after infection with 10^3 CFU of *M. tuberculosis* H37Rv (*M. tuberculosis*). All cavities appeared between 14 and 28 days (Figure 1D) and were large in volume (Figure 1E). Histologically, the cavities were similar to human cavities, comprising a fibrotic wall surrounding a necrotic core (Figures 1F and G). Numerous acid-fast bacilli were present within the necrotic debris (Figure 1H). Several other histopathologic features typical of human TB also developed. These included: (i) small paucibacillary cellular granulomas which were observed in the tissue surrounding the cavity, at sites distal to the cavity, and occasionally in lobes that were not directly infected (Figure 1I and Supplementary Figures 1 and 2), (ii) multinucleated giant cells at the periphery of cavitary lesions (Figure 1J), and (iii) direct connection of the cavity to the bronchi (Figure 1B and Supplementary Figure 1).

Cavities contain high bacillary burdens

Next, we investigated the association between radiographic findings, pathology and bacterial burden. CT appearances were strongly representative of gross pathology (Figure 2A). The majority of the bacterial burden was within the lobe containing the cavity (Figure 2B). We investigated the precise location of the maximal bacterial burden and obtained multiple biopsies from the cavity wall, the surrounding granulomatous material (in the same lobe), and from normal-appearing tissue in the lobe which was adjacent to the initially infected lobe, but in the contralateral lung of each animal (Supplementary Figure 2). Quantitative culture demonstrated an approximately 100-fold increase of bacterial burden at the cavity

surface when compared to the granulomatous regions ($p<0.001$) (Figure 2C). Acid-fast staining of these regions confirmed that bacteria were located within the necrotic debris at the cavity surface, whereas the remaining lung pathology was paucibacillary, with very few acid-fast bacilli visualized within granulomas (Supplementary Figure 2).

Tissue destructive MMPs are abundant at the cavity surface

Having demonstrated histological similarity to human disease, we sought to investigate molecular correlates of tissue destruction. We investigated MMPs implicated in tissue destruction during human infection (Supplementary Table 2). Multiple MMPs showed increased transcription in regions of pathological change in pulmonary architecture, including MMP-1, -3, -7, -12, and -13, (Figures 3A and B). MMP-1 (interstitial collagenase) showed the greatest fold increase in transcription and was the only MMP investigated that was more highly expressed in cavity walls as compared to granulomatous tissue ($p<0.01$). The specific inhibitor TIMP-3 had lower expression in cavity as compared to non-cavity tissue ($p<0.001$) (Figure 3C). Because MMP-1 is highly implicated as both a marker of disease progression and cavitation in man [15], we sought to confirm that its increased transcription correlated with protein abundance. We demonstrated a nearly 10-fold increase in MMP-1 protein concentration around the cavity (Figure 3D). Furthermore, MMP-1 proteolytic activity was detected in infected lung tissue (Figure 3E), which was inhibited by incubation with the collagenase inhibitor Ro32-3555 (Cipemastat) (Figure 3F).

In vivo imaging demonstrates that cavitation originates from dense consolidation

To investigate the sequence of events that lead to cavity formation, we performed longitudinal image analysis of *M. tuberculosis*-infected rabbits (Figures 4A–H). Initial bronchoscopic infection caused localized consolidation (Figure 4B), which became less diffuse over the following 7 days (Figure 4C). Subsequently, dense consolidation formed, and then cavitation occurred rapidly within the regions of dense consolidation. In the majority of cases cavities appeared and reached their maximum size within a 7-day period (figure 4D and 4E). The first cavities appeared by day 21, and all animals cavitated by day 28. After formation, cavities remained relatively stable in size (Figures 4E and F), although some resolution occasionally occurred by day 49 (Figure 4G).

Breath-hold CT scanning permits quantification of dynamic changes in pulmonary architecture

To perform detailed quantitative measurement of lung infiltration, we constructed a bio-safety level-3 (BSL-3) respiratory support device, and developed a breath-hold scanning methodology (supplementary figure 3). The system permitted accurate measurement of overall volumes of tissue within given density ranges. The lower pressure represents an approximately normal inhalation volume, while the higher pressure causes expansion of the lung to beyond physiological norms, allowing the identification of poorly inflated regions that remained consolidated even with this increased expansion (higher-pressures allows for even greater expansion, but was not used to reduce the effect of barotrauma). Two scans of each animal were taken before infection and at day 21, 28, and 35, at inflation pressures of $10cmH_2O$ (lower-pressure) and $20cmH_2O$ (higher-pressure).

Higher-pressure expansion (n=54) led to highly consistent distribution of tissue densities (Figure 4H). We observed an increase in poorly aerated (−100 to 100HU) and hyperexpanded (−1000 to −900HU) tissue volumes, corresponding to consolidation and cavitary change respectively, during the course of infection (Figure 4I).

Assessment of lung consolidation facilitates the estimation of functional lung tissue

We then assessed whether lung consolidation after infection could be measured non-invasively and if the pressure changes permitted measurement of functional tissue. First, we assessed lung recruitment by comparing lung consolidation between the lower and higher inflation pressure measurements. Functional lung tissue decreased significantly after infection and continued to fall until day 35 post-infection (Figure 5B).

Low-density pathological change includes both cavitary and hyperexpansive pathology

Next, we analyzed the CT images to differentiate specific pathological changes driven by *M. tuberculosis* infection in our model. This was achieved by comparing the proportion of voxels at all densities before and after infection, in the more consistent high-pressure scans. A proportion of voxels containing very low-density tissue, (−1022 and −865HU, peak −889HU), representing cavity formation, and a proportion of voxels containing high-density tissue, (−719 to 212HU, peak 35.19HU), representing dense consolidation, showed significant increases (Figure 5C). Conversely, the proportion of tissues (−866 to −712HU, peak −715HU), within the normal aerated range, was reduced. Although the high-density peak was across a broad range of HU, 47% of this peak was in the non-aerated range −100 to 100HU, with the remainder of the peak being evenly distributed from −700 to −100HU.

First, we focused on the low-density peak. Unexpectedly the distribution of voxels was different between the two inflation pressures, with a bifid peak in this region (−1022 to −865HU) (Figure 5C), occurring at high-pressure expansion (Supplementary Figure 6A). To investigate the cause of this phenomenon, we identified a cavity specific region by comparing scans of animals from day 21 and found a significant change in very low density regions (−1024 to −924HU) (Supplementary Figure 6B) that was diagnostic of cavity formation in higher-pressure scans (Supplementary Figure 6C). By further evaluating the distribution of the remaining portion of the bifid peak in 3D-reconstructions (−924 to −865HU; Supplementary Figures 6E and 6F), we established that after infection, a diffuse increase in low-density regions was occurring (Figures 6E and F). This indicates that additional lung hyperexpansion was occurring after infection when lungs were highly inflated.

TB-driven lung inflammation can be quantified accurately

The change in volume of dense tissue was small when expressed as a proportion of total lung voxels, but represented a significant change from baseline (Figures 4I and 5A). Since cavities appear to originate in these dense tissues, and these same areas are unlikely to facilitate gas exchange, we investigated the progression of these regions over time. The region of unique change in proportional volume between pre- and post-infection was identified (−84 to 56HU, Supplementary Figure 7A). The change in volume of these high-density regions was small, but this relatively low volume represents a substantial tissue

mass. We analyzed the mass of high-density tissue pre- and post-infection and identified a larger zone from −184 to +156HU, which demonstrated consistently increasing volume after infection (Supplementary Figure 7B). By highlighting this zone in 3D-reconstructions, we demonstrated that these loci represented areas of new tissue consolidation (Figure 5D).

Both cavitation ($p<0.01$, Figure 5E) and consolidation signatures ($p<0.05$, Figure 5F) within the TB lesions increased progressively during the early stages after infection (days 21–35). Interestingly, both the mass and volume of the regions of consolidation did not decrease during the appearance of cavitation, suggesting that while cavitation originates in these areas, cavities do not lead to a substantial reduction in consolidated tissue. We used the combined volumes of both cavitary and consolidated tissues to generate a total disease score. This score changed substantially between day 21 and 35 of infection ($p<0.001$, Figure 5G) and correlated strongly with the functional decline in tissue ($p<0.0001$; Supplementary Figure 8).

MMP/TIMP imbalance is a bacterial-driven signature of active TB

UV-irradiated *M. tuberculosis* induced substantial level of MMP-1, -3 and -7 expression (Figure 6A) from human blood-derived monocyte macrophages. The addition *M. tuberculosis* culture supernatant significantly enhanced MMP-1 and -3 secretion, but not MMP-7 (Figure 6A). Finally, we took a hypothesis-driven approach to evaluating MMP/TIMP imbalances in peripheral blood from a cohort in India including pulmonary TB (PTB), latent TB (LTBI) and healthy controls (HC) previously used to investigate biomarkers for of active PTB diagnosis [[28], and *Andrade et al.* unpublished data]. We showed that MMP-1/TIMP1-4 ratios were greater in pulmonary TB (PTB) patients than LTBI and healthy controls (Figure 6B). We then utilized hierarchal clustering of tissue degrading MMPs and TIMPs to assess the associations between MMP/TIMP levels and patients with active TB (Figure 6C). Overall increases in MMP-1, -8 and -9 were observed (figure 6D) and a Canonical Correlation Analysis (CCA) model confirmed that peripheral MMP/TIMP imbalance is a prominent feature of active disease (Figure 6E–F).

Discussion

The majority of the global TB burden occurs in immunocompetent adults, where tissue destruction and consequent cavity formation is associated with treatment failure, the emergence of drug resistance, transmission of infection, morbidity, mortality and long-term respiratory impairment [1, 8, 10, 11, 30, 31]. Despite its clinical significance, pulmonary cavitation is poorly understood and the effect of therapeutics in cavitary TB is not established in preclinical trials. To address this gap, we have developed a novel rabbit model of pulmonary cavitation and an imaging strategy that provides objective, quantitative, real-time measure of disease. We demonstrate that cavities develop rapidly from areas of dense consolidation facilitating massive bacterial proliferation in the context of a protease-antiprotease imbalance.

Our model replicates the classical pathology observed in human TB, including cavity and granuloma formation, in a rapid and reliable manner (Figures 1 and 2). These pathologies develop in the presence of the characteristic DTH responses of post-primary TB [13, 32, 33].

TST acts as a functional measure of DTH, as its development is dependent not only on $CD4^{+ve}$ T-cell responses, but also the subsequent recruitment and activation of monocytes, NK Cells and $CD8^{+ve}$ T cells, as well as IFNγ and Il-12 mediated inflammatory cascades [12]. Pre-existing DTH to *M. tuberculosis* is common in endemic regions where 90% of healthy adults are TST-positive [33]. In low prevalence settings, where population prevalence of TST-positivity is low, TST-positivity is present in 90% of individuals with active TB [32]. Experimental data from rabbits indicate that DTH, as measured by any induration of TST, either from pre-sensitization, or through prolonged infection, predicts cavity formation [24, 25, 29, 34]. By recapitulating post-primary DTH, our model rapidly generates cavities which are highly representative of human pathology: there is a fibrotic layer surrounded by monocytes, within which lies a layer of epithelioid macrophages which are progressively more necrotic towards the center of the cavity, that contains high numbers of culturable, acid-fast bacilli [5, 12, 13]. This model compliments existing mouse, guinea-pig, rabbit and non-human primate models, adding to their utility in the study of multiple drug regimens, vaccine efficacy, granuloma progression and human-like immune responses respectively, the possibility of studying cavitary disease preclinically [29, 35–37].

Clinical studies can only provide a snapshot of disease progression and consequently do not inform us of the precise sequence of events during cavity formation. To address this, we developed novel methods to accurately quantify tissue destruction *in vivo* (Figures 4 and 5). Previously, positron emission tomography (PET) using the glucose analogue 2-deoxy-2-[^{18}F]fluoro-D-glucose (^{18}F-FDG) has been used in clinical and preclinical trials [38–40]. In comparison to PET, CT scanning has several key technical benefits: CT gives detailed structural information, does not require intravenous injections, does not use radioisotopes, can be acquired in less than 30 seconds, allows for high-resolution (in this case, 0.5×0.5×0.625mm) quantitation, and is more readily available [41, 42]. Previous CT analyses have primarily focused on pattern recognition, and to date, no technique to quantitatively assess TB disease severity by CT has been developed [43–46]. Hunter's exhaustive review of human specimens and post-mortem studies indicated that cavities emerge from regions of confluent consolidation, and not from individual granulomas [5]. Our model recapitulates this process, revealing that cavitation is a very rapid process. Further studies are required to determine the exact nature of the pre-cavitary lesion.

Pulmonary extracellular matrix (ECM) is highly resilient, and its rapid destruction requires proteolytic enzymes [47, 48]. Previous studies have identified correlates between active TB and increased MMP expression in respiratory secretions, but not a direct link between cavity formation and MMP activity [15, 16, 18]. In this study, we established a unique and specific relationship between MMP-1 expression and cavitary pathology (Figure 3). Our finding that in rabbits, MMP-1, -3, -7, -12 and -13 transcriptional levels are increased in granulomatous and cavitary pathologies correlate with the finding that several of these MMPs are increased in human respiratory secretions and *in vivo* models [16, 49]. TIMP-1 did increase in our model, although not substantially, a finding also consistent with human data [18]. The reduction in TIMP-3 is predicted by *in vitro* human monocyte infection models, but has not been observed in tissue [27]. TIMP-3 deficiency in mice is, in isolation sufficient to lead to

lung ECM degradation [50]. This suggests that, in rabbits, MMP-1/TIMP-3 imbalance is specifically associated with cavity formation.

Previously, we have demonstrated that MMP-1 and -3 expression is greater in macrophage infected with pathogenic *M. tuberculosis* than attenuated vaccine strains [27]. We provide evidence that secreted and cellular components of *M. tuberculosis* drive the collagen degrading MMP-1, and its activator MMP-3 but not non-collagenolytic MMPs (Figure 6A). This evidence from the rabbit and macrophage infection models, as well as previous studies indicate that MMP/TIMP imbalance is a key feature of cavity disease [18].

Our final evaluation was of the diagnostic potential of MMP/TIMP imbalances in human plasma. Prior studies used induced sputum or bronchoalveolar lavage samples, which are not easily attainable diagnostic materials. In this study we utilized plasma, which is easier to attain and process. We first confirmed that MMP-1/TIMP imbalance was significantly altered in active disease (Figure 6B), and demonstrate that although MMP/TIMP imbalances alone are not diagnostic of active disease; they have potential as peripheral markers of active pulmonary TB (Figure 6E–F).

In summary, our model, in combination with previous studies of both human and rabbit disease, suggests that DTH reactions as well as MMP/TIMP imbalances are key components of cavity development [15, 24]. Through direct observation of cavitation, we reveal that dense consolidation erodes to leave a cavity in which bacterial multiplication is unchecked the airways can be accessed (supplementary figure 1). We provide evidence that a bacterial-driven host-protease imbalance drives cavity formation. The protease-antiprotease imbalance distinguishes active from latent disease in man. Although not of diagnostic power, this may be relevant to screening or diagnostic pathways. We predict that restoration of this imbalance may be of benefit in TB treatment. Our model provides a strategy for investigating protease directed (and other) therapies in the context of human-like pathology. Such studies will provide: (i) mechanistic insight into TB pathogenesis (ii), the function of the targeted pathways in immunity and (iii), the therapeutic potential of these drugs as adjunctive TB therapy.

Supplementary Material

Refer to Web version on PubMed Central for supplementary material.

Acknowledgments

WRB acknowledges the support of Howard Hughes Medical Institute and NIH grants R01 AI 079590; R01 AI037856, and R01 AI036973. AK and JSF were supported by a grant from Imperial College London. SKJ was supported by NIH Director’s New Innovator Award DP2-OD6492 and R01-HL116316.

References

1. Global tuberculosis report 2013. World Health Organization; 2013. Report No.: 9789241564656
2. Laxminarayan, R.; Klein, E.; Dye, C., et al. Economic benefit of tuberculosis control. 2007.
3. Global tuberculosis report 2010. World Health Organization; 2010. Report No.: WHO/HTM/TB/2010.7

4. Hatipoglu ON, Osma E, Manisali M, et al. High resolution computed tomographic findings in pulmonary tuberculosis. Thorax. 1996; 51:397–402. [PubMed: 8733492]
5. Hunter RL. Pathology of post primary tuberculosis of the lung: An illustrated critical review. Tuberculosis. 2011; 91:497–509. [PubMed: 21733755]
6. Elkington PT, Armiento JM, Friedland JS. Tuberculosis immunopathology: the neglected role of extracellular matrix destruction. Science Translational Medicine. 2011; 3:71ps76–71ps76.
7. Canetti, G. The Tubercle Bacillus in the Pulmonary Lesion of Man. 1955. p. 226
8. Golub JE, Bur S, Cronin WA, et al. Delayed tuberculosis diagnosis and tuberculosis transmission. International Journal of Tuberculosis and Lung Disease. 2006; 10:24–30. [PubMed: 16466033]
9. Kaplan G, Post FA, Moreira AL, et al. *Mycobacterium tuberculosis* growth at the cavity surface: a microenvironment with failed immunity. Infection and Immunity. 2003; 71:7099–7108. [PubMed: 14638800]
10. Benator D, Bhattacharya M, Bozeman L, et al. Rifapentine and isoniazid once a week versus rifampicin and isoniazid twice a week for treatment of drug-susceptible pulmonary tuberculosis in HIV-negative patients: a randomised clinical trial. Lancet. 2002; 360:528–534. [PubMed: 12241657]
11. Visser ME, Stead MC, Walzl G, et al. Baseline predictors of sputum culture conversion in pulmonary tuberculosis: Importance of cavities, smoking, time to detection and W-Beijing genotype. PloS one. 2012; 7:e29588. [PubMed: 22238625]
12. Kumar, V.; Abbas, AK.; Fausto, N., et al. Robbins and Cotran Pathologic Basis of Disease. 8. Saunders Elsevier; Philadelphia: 2010.
13. Hunter RL, Jagannath C, Actor JK. Pathology of postprimary tuberculosis in humans and mice: Contradiction of long-held beliefs. Tuberculosis. 2007; 87:267–278. [PubMed: 17369095]
14. Dannenberg, AM. Pathogenesis of human pulmonary tuberculosis: Insights from the rabbit model. American Society for Microbiology Press; 2006. p. 453
15. Elkington P, Shiomi T, Breen R, et al. MMP-1 drives immunopathology in human tuberculosis and transgenic mice. The Journal of clinical investigation. 2011; 121:1827–1833. [PubMed: 21519144]
16. Walker NF, Clark SO, Oni T, et al. Doxycycline and HIV infection suppress tuberculosis-induced matrix metalloproteinases. American journal of respiratory and critical care medicine. 2012; 185:989–997. [PubMed: 22345579]
17. Seddon J, Kasprowicz V, Walker NF, et al. Procollagen III N-terminal propeptide and desmosine are released by matrix destruction in pulmonary tuberculosis. Journal of Infectious Diseases. 2013; 208:1571–1579. [PubMed: 23922364]
18. Ugarte-Gil CA, Elkington P, Gilman RH, et al. Induced sputum MMP-1, -3 & -8 concentrations during treatment of tuberculosis. PloS one. 2013; 8:e61333. [PubMed: 23613834]
19. Pais TF, Silva RA, Smedegaard B, et al. Analysis of T cells recruited during delayed-type hypersensitivity to purified protein derivative (PPD) versus challenge with tuberculosis infection. Immunology. 1998; 95:69–75. [PubMed: 9767459]
20. Leong, FJ.; Dartois, V.; Dick, T. A Color Atlas of Comparative Pathology of Pulmonary Tuberculosis. CRC Press; 2010.
21. McMurray, DN.; Collins, FM.; Dannenberg, AM., Jr, et al. Pathogenesis of Experimental Tuberculosis in Animal Models. In: Shinnick, T., editor. Tuberculosis. Springer; Berlin Heidelberg: 1996. p. 157-179.
22. Kjellsson MC, Via LE, Goh A, et al. Pharmacokinetic evaluation of the penetration of antituberculosis agents in rabbit pulmonary lesions. Antimicrobial Agents and Chemotherapy. 2011; 56:446–457. [PubMed: 21986820]
23. Green AM, Mattila JT, Bigbee CL, et al. CD4+ regulatory T cells in a cynomolgus macaque model of *Mycobacterium tuberculosis* infection. Journal of Infectious Diseases. 2010; 202:533–541. [PubMed: 20617900]
24. Nedeltchev GG, Raghunand TR, Jassal MS, et al. Extrapulmonary dissemination of *Mycobacterium bovis* but not *Mycobacterium tuberculosis* in a bronchoscopic rabbit model of cavitary tuberculosis. Infection and Immunity. 2009; 77:598–603. [PubMed: 19064634]

25. Jassal MS, Nedeltchev GG, Osborne J, et al. A modified scoring system to describe gross pathology in the rabbit model of tuberculosis. BMC microbiology. 2011; 11:49. [PubMed: 21375756]
26. Gattinoni L, Caironi P, Cressoni M, et al. Lung recruitment in patients with the acute respiratory distress syndrome. New England Journal of Medicine. 2006; 354:1775–1786. [PubMed: 16641394]
27. Elkington PTG, Nuttall RK, Boyle JJ, et al. *Mycobacterium tuberculosis*, but not vaccine *BCG*, specifically upregulates matrix metalloproteinase-1. American journal of respiratory and critical care medicine. 2005; 172:1596–1604. [PubMed: 16141443]
28. Andrade BB, Pavan Kumar N, Mayer-Barber KD, et al. Plasma heme oxygenase-1 levels distinguish latent or successfully treated human tuberculosis from active disease. PLoS ONE. 2013; 8:e62618. [PubMed: 23671613]
29. Subbian S, Tsenova L, Yang G, et al. Chronic pulmonary cavitary tuberculosis in rabbits: a failed host immune response. Open Biology. 2011; 1:110016. [PubMed: 22645653]
30. Menezes AMB, Hallal PC, Perez-Padilla R, et al. Tuberculosis and airflow obstruction: evidence from the PLATINO study in Latin America. European Respiratory Journal. 2007; 30:1180–1185. [PubMed: 17804445]
31. Hnizdo E, Singh T, Churchyard G. Chronic pulmonary function impairment caused by initial and recurrent pulmonary tuberculosis following treatment. Thorax. 2000; 55:32–38. [PubMed: 10607799]
32. Huebner RE, Schein MF, Bass JB Jr. The tuberculin skin test. Clinical Infectious Diseases. 1993; 17:968–975. [PubMed: 8110954]
33. Wood R, Liang H, Wu H, et al. Changing prevalence of tuberculosis infection with increasing age in high-burden townships in South Africa. The International Journal of Tuberculosis and Lung Disease. 2010; 14:406–412. [PubMed: 20202297]
34. Converse PJ, Dannenberg AM Jr, Estep JE, et al. Cavitary tuberculosis produced in rabbits by aerosolized virulent tubercle bacilli. Infection and Immunity. 1996; 64:4776–4787. [PubMed: 8890239]
35. Lanoix J-P, Betoudji F, Nuermberger E. Novel regimens identified in mice for treatment of latent tuberculosis infection in contacts of patients with multidrug-resistant tuberculosis. Antimicrobial Agents and Chemotherapy. 2014; 58:2316–2321. [PubMed: 24492372]
36. Horwitz MA, Harth G. A new vaccine against tuberculosis affords greater survival after challenge than the current vaccine in the guinea pig model of pulmonary tuberculosis. Infection and Immunity. 2003; 71:1672–1679. [PubMed: 12654780]
37. Kunnath-Velayudhan S, Davidow AL, Wang H-Y, et al. Proteome-scale antibody responses and outcome of *Mycobacterium tuberculosis* infection in nonhuman primates and in tuberculosis patients. The Journal of infectious diseases. 2012; 206:697–705. [PubMed: 22732925]
38. Lee M, Lee J, Carroll MW, et al. Linezolid for treatment of chronic extensively drug-resistant tuberculosis. New England Journal of Medicine. 2012; 367:1508–1518. [PubMed: 23075177]
39. Davis SL, Nuermberger EL, Um PK, et al. Noninvasive pulmonary [18F]-2-fluorodeoxy-D-glucose positron emission tomography correlates with bactericidal activity of tuberculosis drug treatment. Antimicrobial Agents and Chemotherapy. 2009; 53:4879–4884. [PubMed: 19738022]
40. Lin PL, Coleman T, Carney JPJ, et al. Radiologic responses in cynomolgous macaques for assessing tuberculosis chemotherapy regimens. Antimicrobial Agents and Chemotherapy. 2013
41. Uchiyama Y, Katsuragawa S, Abe H, et al. Quantitative computerized analysis of diffuse lung disease in high-resolution computed tomography. Medical Physics. 2003; 30:2440–2454. [PubMed: 14528966]
42. Xu Z, Bagci U, Kubler A, et al. Computer-aided detection and quantification of cavitary tuberculosis from CT scans. Medical Physics. 2013; 40:113701. [PubMed: 24320475]
43. Cha J, Lee HY, Lee KS, et al. Radiological findings of extensively drug-resistant pulmonary tuberculosis in non-AIDS adults: comparisons with findings of multidrug-resistant and drug-sensitive tuberculosis. Korean Journal of Radiology. 2009; 10:207–216. [PubMed: 19412508]

44. Yeh JJ, Chen SC-C, Teng W-B, et al. Identifying the most infectious lesions in pulmonary tuberculosis by high-resolution multi-detector computed tomography. European Radiology. 2010; 20:2135–2145. [PubMed: 20432040]
45. Genereux GP. Pattern recognition in diffuse lung disease. A review of theory and practice. Medical radiography and photography. 1985; 61:2–31. [PubMed: 2995759]
46. Sider L, Gabriel H, Curry DR, et al. Pattern recognition of the pulmonary manifestations of AIDS on CT scans. Radiographics: a review publication of the Radiological Society of North America, Inc. 1993; 13:771–784. discussion 785–776.
47. Petersen TH, Calle EA, Zhao L, et al. Tissue-engineered lungs for *in vivo* implantation. Science. 2010; 329:538–541. [PubMed: 20576850]
48. Loffek S, Schilling O, Franzke CW. Series “matrix metalloproteinases in lung health and disease”: Biological role of matrix metalloproteinases: a critical balance. European Respiratory Journal. 2011; 38:191–208. [PubMed: 21177845]
49. Singh S, Saraiva L, Elkington PT, et al. Regulation of matrix metalloproteinase-1, -3, and -9 in *Mycobacterium tuberculosis*-dependent respiratory networks by the rapamycin-sensitive PI3K/p70(S6K) cascade. FASEB J. 2014; 28:85–93. [PubMed: 24076964]
50. Leco KJ, Waterhouse P, Sanchez OH, et al. Spontaneous air space enlargement in the lungs of mice lacking tissue inhibitor of metalloproteinases-3 (TIMP-3). The Journal of clinical investigation. 2001; 108:817–829. [PubMed: 11560951]

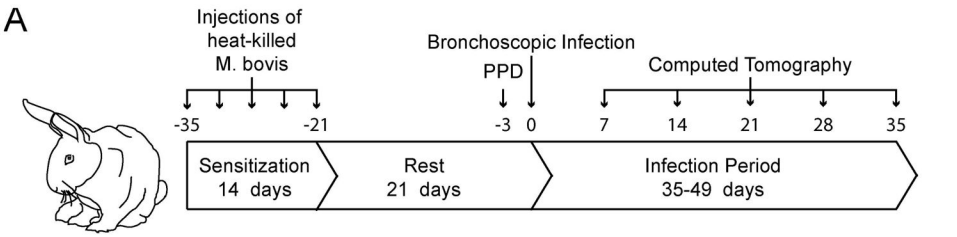

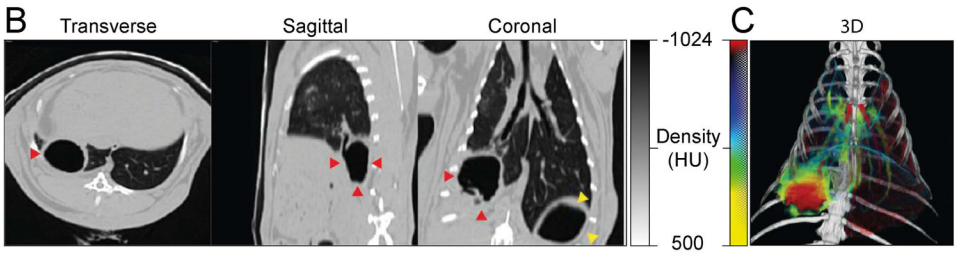

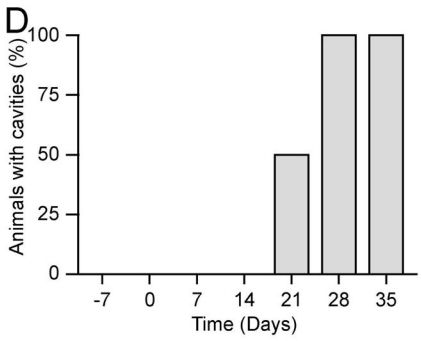

E

Rabbit	Maximum Cavity Volume (cm^3)	Rabbit	Maximum Cavity Volume (cm^3)
A	2.99	G	7.79
B	2.91	H	2.59
C	6.86	I	3.15
D	0.70	J	2.96
E	7.67	K	2.63
F	3.25	L	9.18

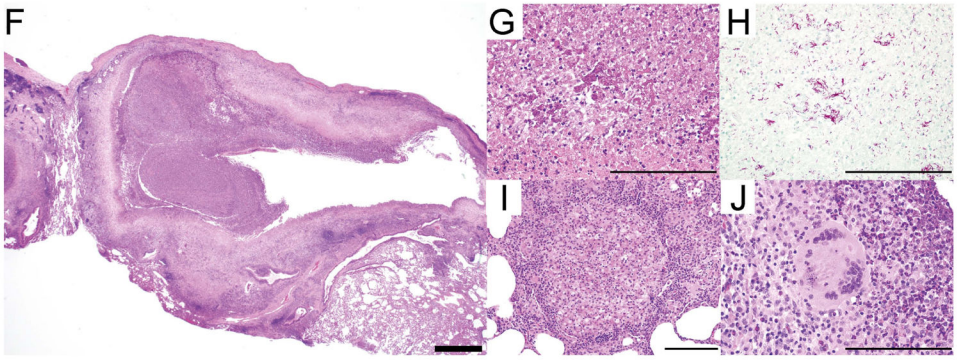

Figure 1. A reproducible model of TB which demonstrates human-like pathology and cavity formation within 28 days

(A) Sensitization and infection protocol: Rabbits were sensitized by administering 5 injections over 14 days, each containing 10^8 heat-killed CFU of *M. bovis* strain Ravenel. After 21 days, PPD testing was performed to confirm the development of delayed-type hypersensitivity to *M. tuberculosis* complex antigens. Infection with 10^3 CFU of *M. tuberculosis* was then performed 3 days after PPD testing under bronchoscopic guidance. The animals were monitored by serial CT imaging and then humanely sacrificed at pre-determined time points. See methods for detailed description. (B) Representative CT scan of a rabbit with a cavity. Red arrows indicate the cavity, while yellow arrows indicate gastric air. (C) A 3D-reconstruction of a representative animals scan using a customized scale in

which low density regions (cavities and airways) are represented in red, and high density regions (blood vessels and consolidation) in a green to yellow scale where yellow regions are more dense. (D) Proportion of animals with cavities at each time point as assessed by CT scan (n=12). (E) Cavity size was assessed using an automated cavity segmentation algorithm [ref. 45]. Maximum cavity sizes for each animal are shown. (F–J) H+E stained slides of rabbit lung tissue demonstrating all the pathognomic features of human TB: (F) Low power image of cavity, with air-filled center, necrotic rim and a peripheral fibrotic cuff. (G) Necrotic debris at cavity surface (H) Ziehl-Neelsen staining demonstrates numerous bacteria within necrotic debris (I) Small cellular granuloma without central caseation (J) Multinucleate giant cell within granuloma. (Scale bars; F 1mm, G–J 200μm. HU = Hounsfield units).

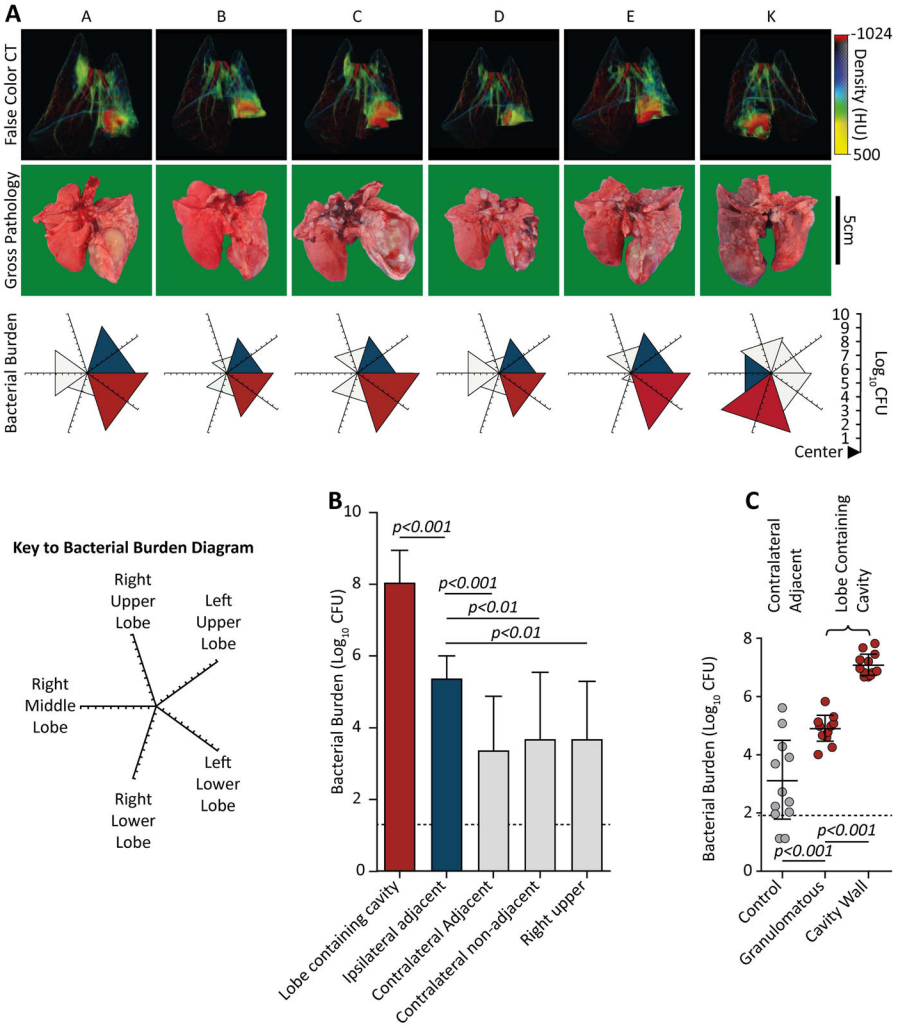

Figure 2. Bacterial burden is 100-fold higher at the cavity surface than in granulomatous lung tissue

(A) Matched findings from 6 animals (A–E and K), showing correlations between pre-mortem CT scans, post-mortem gross pathology and *M. tuberculosis* burden. CT scans reliably demonstrate the lobe containing the cavity. The bacterial burden is represented on a 5-directional axis with each axis representing a lobe of the rabbit lung. Bacterial burden is highest in the lobe with most extensive pathology. (B) The majority of the bacteria are found within the cavitary lobe (n=12). (Red; lobe containing cavity, blue; ipsilateral adjacent [relative to cavity] lobe, light gray; non-adjacent [to cavity] lobes, no triangle; no bacilli cultured). (C) Bacterial burden within the cavitary lobe was assessed by taking 3mm punch biopsies from the surface of the cavity, non-cavity infected tissue from the same lobe, and tissue the contralateral lower lobe (6 samples per region per animal, n=11). The bacterial burden is almost exclusively at the cavity surface, representing 99.9% of bacteria. (Error bars represent standard deviation, p-values calculated using one-way ANOVA with Tukey post-comparison test).

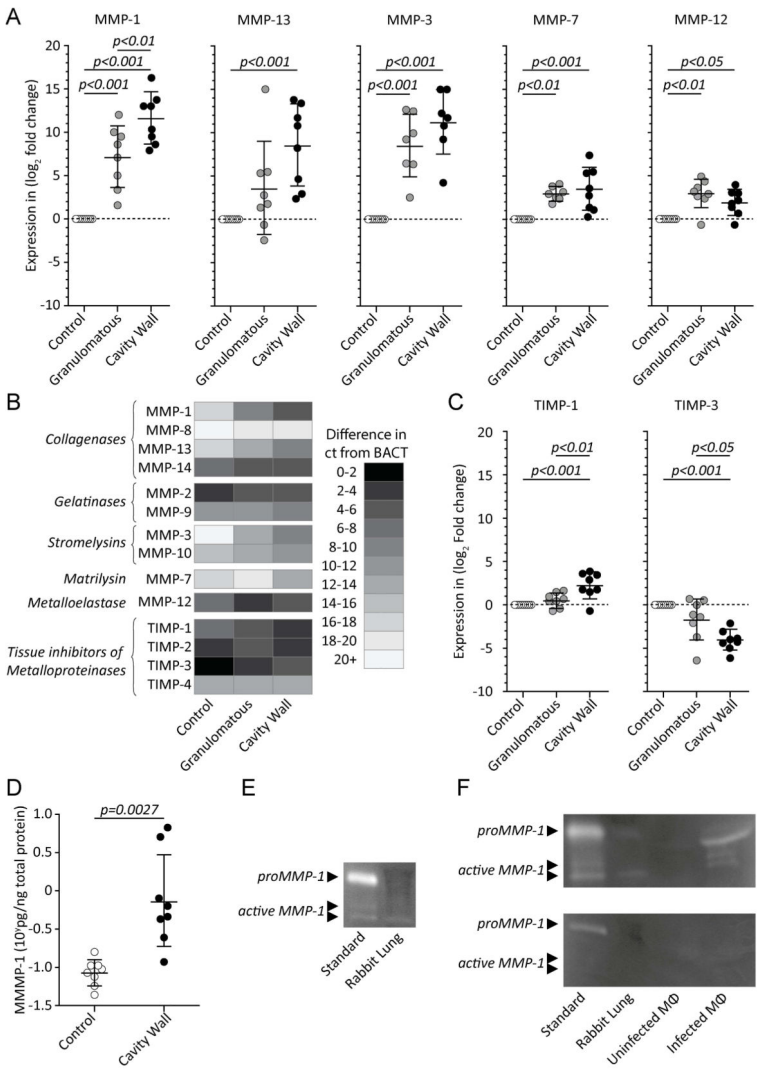

Figure 3. Tissue-destructive MMPs are upregulated in infected lung, in particular within the cavity wall

(A) Multiple MMPs implicated in human TB immunopathology are upregulated in infected lung tissue when evaluated by q-RT PCR. (B) Heat chart showing approximate MMP expression levels as evaluated by average difference in ct-value relative to beta actin (BACT). (C) TIMP-1 and TIMP-3 expression in cavity wall, granulomatous and normal tissue. (D) MMP-1 protein concentration analyzed by ELISA demonstrated a significant increase in cavity wall as compared to normal tissue. (E) MMP-1 activity was demonstrated by casein zymography, with a band of proteolytic activity at 35kDA in infected lung tissue similar to active recombinant MMP-1. (F) Ro32-3555 completely inhibits caseinolytic activity of both *M. tuberculosis* infected rabbit lung tissue and human macrophages (mφ) infected with *M. tuberculosis*. (Error bars represent standard deviation, ct; cycle threshold, p-values calculated using one-way ANOVA with Tukey post-comparison test).

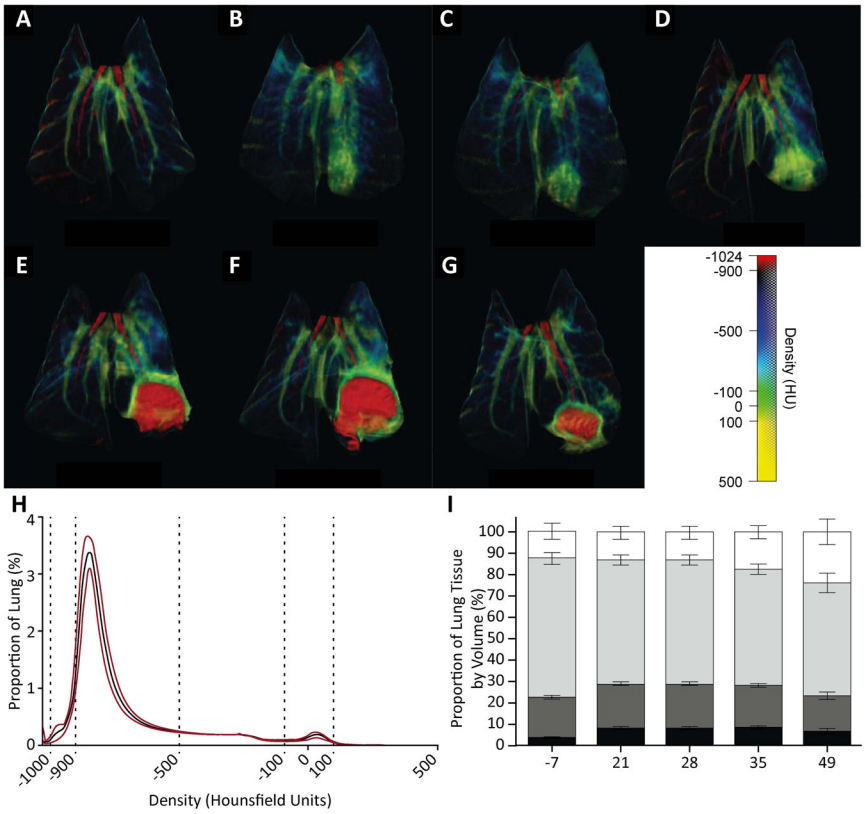

Figure 4. 3-dimensional false-color reconstruction of CT images demonstrates disease progression over time

(A–G) Serial imaging of a single, representative rabbit over 49 days. Day 7 and 14 are non-anesthetized, non-breath-hold scans, all others are breath-hold scans with the lungs inflated to 20cmH_2O inflation. (H) Proportional distribution of pulmonary tissue by density when inflated to 20cmH_2O of pressure demonstrates highly reproducible density spectrum (n=54). Black line represents mean density and red lines represent standard deviation. (I) Proportional distribution of voxels inflated to 10cmH2O, grouped by tissue type derived from Hounsfield Units (HU). (Black, not inflated, −100 to 100HU; Dark Grey, poorly aerated, −101 to −500HU; light grey, normally aerated, −501 to −900HU; white, hyperexpanded, −901 to −1000HU. Error bars represent standard deviations).

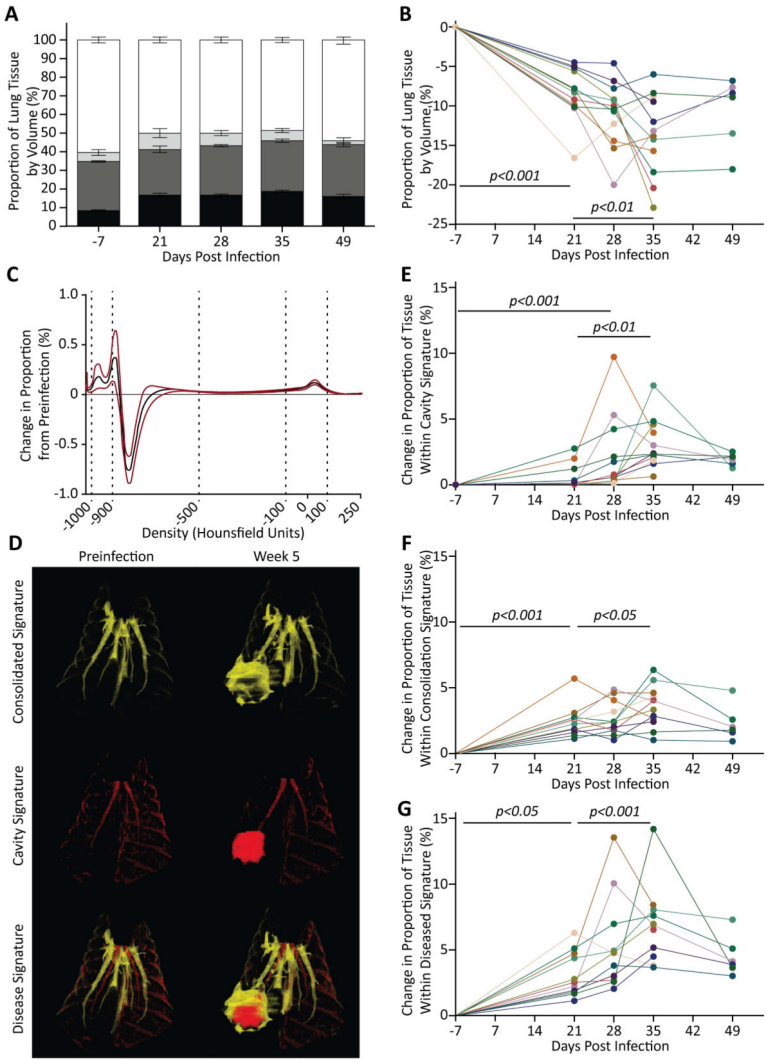

Figure 5. Disease progression in individual animals can be quantitatively analyzed *in vivo*

(A) Distribution of tissue mass in lungs, inclusive of tissue recruited during expansion from 10cmH_2O to 20cmH_2O scans (Black, not aerated; darkest grey, poorly aerated; middle grey, potentially recruited; light grey, normally aerated; white, hyperexpanded). (B) Proportional loss of functional lung tissue by mass during the course of infection. Functional tissue is sum of normally aerated tissue and potentially aerated tissue. (C) Change in proportional voxel density distribution after infection (n=42). (D) Visualization of pathological changes using. Yellow, high density, consolidation, −184 to +156HU; red, low density, cavity, −1024 to −924HU. (E–G) *In vivo* quantification of pulmonary pathological change. (E) Proportion of lung containing a cavity signature to day 35 post infection. (F) Proportion of lung containing a consolidation signature. (G) Overall diseased lung signature, incorporating both consolidated and cavitary tissue. (p-values calculated using repeated-measures ANOVA with Tukey post-comparison test).

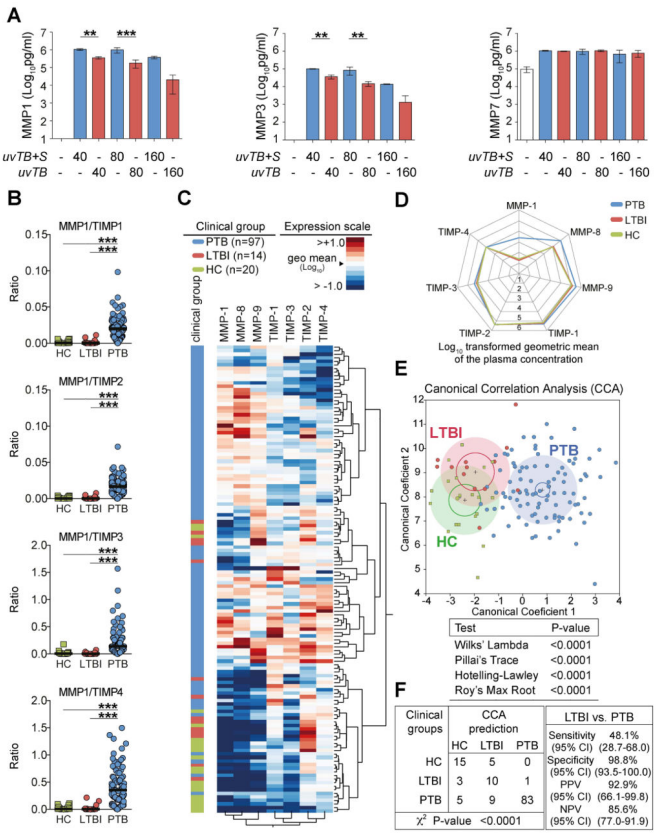

Figure 6. MMP/TIMP imbalance in humans

(A) MMP-1/-3 and -7 levels were measured in supernatant from human monocyte derived macrophages infected with UV-killed *M. tuberculosis* in the presence or absence of released bacterial products. (B) Plasma concentrations of several MMPs and TIMPs were assessed by ELISA in samples from ATT-naïve active pulmonary TB patients (PTB, n=97), individuals with latent TB infection (LTBI, n=14) and age and gender matched healthy controls (HC, n=20). The ratio between levels of MMP-1 and each one of the TIMPs are shown. (C) An unsupervised two-way clustering analysis (Ward's method) was employed using the plasma concentrations of each MMP and TIMP. Individuals from the PTB, LTBI or HC groups were listed in rows and each biomarker was placed in a different column. The squares in the heat map represent values below or above the geometric mean values (log10 transformed) of a given biomarker in the entire study population (n=131), with dark red indicating an increase in expression and dark blue a decrease. (D) A representative profile of geometric mean values (log10 transformed) for MMPs and TIMPs in plasma is shown for each clinical group. (E) The performance of the combined assessment of plasma concentrations of several MMPs and TIMPs in distinguishing the different clinical groups was tested using a Canonical Correlation Analysis (CCA) model. The statistically significance of the CCA model was tested using standardized tests and P values for each one of them is shown. Small circles represent the 95% confidence region to contain true mean of each group whereas large shaded ellipses represent region estimated to contain 50% of the population of each group. (F) The performance of the CCA model in distinguishing the different clinical groups as well as details of sensitivity, specificity and predictive values of the test distinguishing

PTB form LTBI are shown. In (B), data were analyzed using Kruskal-Wallis test with Dunn's multiple comparisons post hoc test. In F, data was analyzed using chi-square (left panel) and the Fisher's exact tests (right panel) ***P<0.0001; CI, confidence interval.